High Performance Computing Algorithms for Land Cover Dynamics Using Remote Sensing Data

Satya Kalluri[1] Joseph JáJá[2] David A. Bader[3] Zengyan Zhang[2]
John Townshend[4] Hassan Fallah-adl[2]

Institute for Advanced Computer Studies (UMIACS)
University of Maryland, College Park, MD 20742

December 8, 1998

[1]Department of Geography, University of Maryland, College Park, MD 20742
[2]UMIACS and Department of Electrical Engineering
[3]Electrical and Computer Engineering Dept., University of New Mexico, Albuquerque, NM 87131
[4]UMIACS and Department of Geography

Abstract

Global and regional land cover studies require the ability to apply complex models on selected subsets of large amounts of multi-sensor and multi-temporal data sets that have been derived from raw instrument measurements using widely accepted pre-processing algorithms. The computational and storage requirements of most such studies far exceed what is possible on a single workstation environment. We have been pursuing a new approach that couples scalable and open distributed heterogeneous hardware with the development of high performance software for processing, indexing, and organizing remotely sensed data. Hierarchical data management tools are used to ingest raw data, create metadata, and organize the archived data so as to automatically achieve computational load balancing among the available nodes and minimize I/O overheads. We illustrate our approach with four specific examples. The first is the development of the first fast operational scheme for the atmospheric correction of Landsat TM scenes, while the second example focuses on image segmentation using a novel hierarchical connected components algorithm. Retrieval of global BRDF (Bidirectional Reflectance Distribution Function) in the red and near infrared wavelengths using four years (1983 to 1986) of Pathfinder AVHRR Land (PAL) data set is the focus of our third example. The fourth example is the development of a hierarchical data organization scheme that allows on-demand processing and retrieval of regional and global AVHRR data sets. Our results show that substantial improvements in computational times can be achieved by using the high performance computing technology.

1 Introduction

Global change studies through the use of remote sensing techniques require multidisciplinary research with fusion of data sets from various sources and instruments. Although multitemporal high resolution satellite data has been collected since the early 1970's (e.g. Landsat and Advanced Very High Resolution Radiometer (AVHRR) data sets), routine use of these data sets in modeling global carbon, biogeochemical, and hydrological cycles and ecosystem response to natural and anthropogenic changes at a global scale is hindered by the requirements of tremendous data storage and high computational complexity.

The acquisition, processing, mapping and conversion of remotely sensed data to science products useful for studying land cover dynamics involves addressing a number of complex modeling and computational problems. The computational tasks involved in a variety of pre-processing or "conditioning" of satellite data such as calibration, atmospheric and topographic correction, and identification of clouds consist of a mixture of simple pixel operations and complex neighborhood operations.

As typical examples, we consider Landsat Thematic Mapper (TM) and AVHRR data processing streams to gauge the computational and storage requirements to process level zero to level two products at a global scale, since data from these two instruments has been widely used to study land cover dynamics for more than 15 years (Townshend 1994, Goward and Williams 1997). We estimate that 4,500 TM scenes are required to achieve a global coverage of the land surface, and about 237 Giga Floating Point Operations (GFLOPs) are involved in generating a land cover product from a level zero scene. The total storage requirements for this data would be 2.7 Tbytes and would require 1.06 Peta FLOPs to process. Similarly, to process the entire 17 year archive of Global Area Coverage (GAC) data from AVHRR would require the processing of 4.65 Tbytes of data, which would take 3.5 years to process on a single processor (Acharya et al. 1996). Moreover, significant improvements in processing algorithms could mandate reprocessing of these data sets from time to time to produce enhanced and more accurate measurements of the land surface. It is evident from these examples that we need to resort to high performance computing techniques to achieve the objective of acquiring routine, timely information from earth orbiting satellites.

Under the sponsorship of the National Science Foundation's Grand Challenge Program, we embarked on a comprehensive research program in 1994 on the application of high performance parallel computing to data and computation intensive problems in land cover dynamics. Innovative parallel and scalable algorithms are being developed in a heterogeneous distributed computing environment for rapid and accurate processing of large satellite data sets. The processing procedures that have been developed include:

- Atmospheric correction of TM data

- Image segmentation
- Retrieval of land surface bidirectional reflectance distribution function (BRDF), and
- Designing a database for processing, storing and retrieving AVHRR data.

In this paper we present a summary of results from this work. The following sections briefly describe the results from various algorithms that we have successfully implemented using innovative computational techniques.

2 Atmospheric Correction of TM Data

Remote sensing measurements are contaminated by atmospheric effects such as Rayleigh scattering due to atmospheric molecules, absorption by water vapor, ozone and other gases, and scattering and absorption due to atmospheric aerosols. Unless satellite data is corrected for these effects, large errors could result in measuring the variables required for studying land cover dynamics (Kaufman 1984, Singh and Saull 1988). The atmospheric effect varies spatially and temporally, and is also dependent upon the wavelength and geometry of observations. It is possible to decouple the effects of various individual components in the atmosphere on the remote sensing signal and perform selective corrections (Tanre et al. 1992). For a plane-parallel atmosphere bounded by a lambertian surface, the radiance at the top of the atmosphere can be expressed as (Chandrasekhar 1960, Fraser and Kaufman 1985):

$$L_\lambda = L_0 + \frac{\rho F_d T}{\pi(1 - s\rho)} \tag{1}$$

where L_λ is the radiance recorded by the sensor in wavelength λ, L_0 is the upward radiance at the top of the atmosphere when the surface reflectance (ρ) is zero (path radiance), F_d is the total irradiance at the surface, T is the total transmittance of the atmosphere, and s is the spherical albedo of the atmosphere. Molecular scattering in the atmosphere is well understood, and its effects can be easily corrected (Kaufman and Sendra 1988). Correcting for the aerosol effect is more difficult, since atmospheric aerosols are highly variable in time and space. Atmospheric correction approaches using standard radiative transfer algorithms such as 6S (Vermote et al. 1997) and LOWTRAN7 (Kneizys et al. 1988) require input of atmospheric optical depth data from observations. Moreover, these algorithms perform corrections on single pixel values and are not designed to correct entire scenes.

We have implemented a direct atmospheric correction approach based on the so called "dark target method" of Kaufman and Tanre (1996), and Kaufman and Sendra (1988). Two steps are involved in direct atmospheric correction: estimating optical properties of the atmosphere from the imagery, and retrieving surface reflectance. The principle behind this method is to derive the atmospheric properties by inverting equation (1) from measurements of λ over targets whose ρ is known. Our algorithm is capable of correcting a whole TM scene at once. A step by step approach of the atmospheric correction methodology for TM data is described below (Fallah-Adl et al. 1996a, Fallah-Adl et al. 1996b):

1. For a $w \times w$ window of pixels in the input TM image, dark targets representing dense green vegetation are identified based on a channel 7 reflectance threshold (ρ_7). w typically ranges from 11 to 121, and the default ρ_7 threshold is set at 0.1. Since reflectances in TM channel 7 ($2.08 - 2.35 \mu m$) are least affected by the atmosphere we assume that top of the atmosphere (TOA) reflectances in this channel are equivalent to surface reflectances in the same wavelength. The wavelength intervals of different TM bands are given in Table 1. Both w and ρ_7 can be changed very easily depending upon the scene conditions.

2. If there are several pixels whose ρ_7 is less than the threshold, then their mean value is computed.

3. Reflectances in TM channels 1 (ρ_1) and 3 (ρ_3) for the dark pixels are estimated as (Kaufman et al. 1997):

$$\begin{aligned} \rho_1 &= \rho_7 \times 0.25 \\ \rho_3 &= \rho_7 \times 0.50 \end{aligned}$$

4. Using a precomputed lookup table generated by a radiative transfer code (Fraser et al. 1992) estimate the aerosol optical thickness (τ) in TM bands 1 and 3 from measured and L_{λ_1} and L_{λ_3} for ρ_1, and ρ_3 respectively. i.e. given a surface reflectance and upwelling radiance, estimate τ. τ_1 should be larger than or equal to τ_3. Otherwise, previous steps are repeated with a smaller ρ_7 threshold until $\tau_1 \geq \tau_3$.

5. From τ_1 and τ_3, the aerosol optical thickness in TM bands 2, 4, and 5 are computed using the following exponential relationship between wavelength and aerosol optical thickness:

$$\tau_i = a\lambda_i^{-b}$$

   where τ_i and λ_i are the aerosol optical thickness and central wavelength (μm) in channel i respectively, and $1 \leq i \leq 5$. The coefficients a and b are derived by fitting an exponential curve to τ_1 and τ_3 at wavelengths λ_1 and λ_3 respectively.

6. Once the aerosol optical thickness is determined in all the TM bands, atmospheric correction is applied to the central pixel of the $w \times w$ window using the same look up table. From the measured L_λ and retrieved τ_λ, ρ_λ is estimated.

7. The $w \times w$ window moves in single pixel increments across the image and the above steps are repeated

Liang et al. (1997) validated the aerosol optical thickness values determined by this algorithm from several TM scenes by comparing them with ground observations during the First ISLSCP Field Experiment (FIFE) (Sellers et al. 1992), and the Sulfate Clouds and Radiation Atlantic (SCAR A) experiment (Kaufman and Holben 1996). The correlation between estimated and ground measurements was good (r=0.98). Figure 1a shows a RGB composite of TM bands 1, 2, and 3 from a TM scene over Eastern Maryland, USA, before atmospheric correction, and Figure 1b shows the same scene after atmospheric correction. Most of the atmospheric haze is removed after applying the correction and the image looks clearer than before. The derived aerosol optical thickness values in TM band 1 (blue) are shown in Figure 1c, and the spatial pattern of aerosol optical thickness (Fig. 1c.) is consistent with haze in the image. Optical thickness is higher in the upper left and lower right parts of the image which correspond to areas with dense haze in the original image.

The vertical striping that is observed on either side of the optical thickness image (Fig. 1c) is due to the moving window algorithm used here, and can be explained as follows. If we have a $w \times w$ window, then the central pixel within the window will be $w/2$. A window size of 91×91 was used to correct the image shown in Figure 1. Thus, a full window of 91×91 pixels can only be created around pixels starting from column number 46 to column number $n - 46$, where n is the total number of columns in a two dimensional image(i.e. we have 45 pixels on either side of pixel number 46). The first 45 pixels around which a complete $w \times w$ cannot be created is assigned the optical thickness of the nearest window. Therefore, the column of pixels which are less than $w/2$, and those that are greater than $n - w/2$ present on either side of the image will have a uniform optical thickness which results in striping at the edges.

Our atmospheric correction algorithm was benchmarked on different platforms with serial as well as parallel architectures. Timing results show that it takes 3hrs. 52min. to correct a full TM scene on an IBM RS6000 machine. We have also tested the performance on an IBM SP2 machine which has 16 nodes. Each of these processors on the SP2 have a peak performance of 266 MFLOPS, and are configured with 128 Mbytes of memory and 64Kbytes of cache. All the 16 processors are connected by an Ethernet and a high performance switch that permits all the processors to exchange messages simultaneously. The parallel version of the code is written in the Single Program Multiple Data (SPMD) model, so that all the processors run the same code, but on different parts of the input image simultaneously. For the parallel algorithm, the image is divided in to a number of blocks, and these blocks are distributed equally among all the nodes for processing. The size of the block is dependent upon the memory available to the nodes at the time of processing. On the SP2 configuration described above, atmospheric correction for a full TM scene can be run in 30 minutes (Fallah-Adl et al. 1996a, 1996b), and can in general be shown to achieve a linear speed up as a function of the number of nodes.

These results indicate that a significant reduction in runtime can be achieved by a parallel implementation of the atmospheric correction algorithm, which makes it possible to apply the correction scheme over large areas covered by multiple scenes in a practical manner. Both qualitative and quantitative analysis of several TM scenes corrected by this algorithm show that the results are reliable (Liang et al. 1997). The code has been written in a modular fashion, so that individual components of the correction scheme such as instrument calibration, and the empirical functions relating channel 7, 3 and 1 reflectances can be very easily modified.

3 Image Segmentation Using Hierarchical Connected Components

Segmentation algorithms for remotely sensed imagery cluster pixels into homogeneous regions, which, for example, can be classified into categories with higher accuracy than could be obtained by classifying the individual pixels. Region growing is a class of techniques used in image segmentation algorithms in which, typically, regions are constructed by an agglomeration process that merges pixels to regions when those pixels are both adjacent to the regions and similar in spectral property (e.g. Chang and Li 1994, Haralick and Shapiro 1985, Westman et al. 1990). Each pixel in the scene receives a label from the region-growing process; pixels will have the same label if and only if they belong to the same region. A segmentation process using region-growing techniques may be used to realize a hierarchy of region-labeled images. At the lowest level of the hierarchy, a region contains the set of connected pixels with strict similarity. As we move up the hierarchy, the similarity criteria relaxes and similar regions merge together.

Image segmentation consists of two steps. The first step involves image enhancement and edge detection, and the second step involves identifying uniform regions and labeling them. In region-growing algorithms a region's border is susceptible to erroneous merging at its weakest point, which can be aggravated by several factors, including noise, blur, and lighting. Thus it becomes extremely important to enhance an image before this region-growing process. An ideal image enhancement filter preserves edges as well as smoothes the interior of regions (Bader and JaJa 1996a).

Image enhancement

In remotely sensed imagery, natural regions may have significant variability in each band. Noise, introduced from the scanning of the real scene into the digital domain, will cause single-pixel outliers. Also, illumination and view geometry can cause a gradient of gray levels in pixels across the same region due to surface anisotropy. Because of these and other similar effects, it is necessary to preprocess the image with a stable filter, such as the Symmetric Neighborhood Filter (SNF) that smoothes out the interior pixels of a region to a near-homogeneous level using an iterative technique (Bader and JaJa 1996a, Harwood et al. 1987). Also, due to the point spread function of the instrument, edges of regions are usually blurred (Forster and Best 1994, Poropat 1993) so that the transition in gray levels between regions is not a perfect step over a single pixel, but ramps from one region to the other over several pixels. Most preprocessing filters will smooth the interior of regions at the cost of degrading the edges or, conversely, detect edges while introducing intrinsic error on previously homogeneous regions. The SNF filter is, additionally, an edge-preserving filter that detects blurred transitions and sharpens them while preserving the true border location as best as possible. Therefore, the SNF is an edge-preserving smoothing filter that performs well for simultaneously sharpening edges and smoothing regions. In addition, it is an iterative filter that also can be tuned to retain thin-image structures in remotely sensed imagery corresponding, for example, to rivers and roads.

The SNF enhancement is a stable filter that is applied either for a fixed number of iterations or until stopping criteria (defined below) are reached, and takes the single parameter ϵ, as follows. The SNF filter compares each pixel to its 8-connected neighbors. Note that we are using the notion of 8-connectivity, meaning that two pixels are adjacent if and only if one pixel lies in any of the eight positions surrounding the other pixel (Castleman 1996). Figure 2 shows a diagram of a 3 by 3 neighborhood centered around a pixel, with the symmetric pairs having the same letter. The neighbors are inspected in symmetric pairs around the center, that is, top with bottom, left with right, upper-left with lower-right, and upper-right with lower-left. Assume without loss of generality that the pair of pixels have brightness intensities A and A' and that $A > A'$. Using each pair and the center pixel, four different comparisons are made using the following criteria (Figure 3):

- If the center pixel (with value x) falls within region R_A, that is, $\frac{A+A'}{2} < x \leq A + \epsilon$, then we select A, where $\epsilon = \kappa\sigma^*$. σ^* is the median of the standard deviations of all 3×3 neighborhoods centered around each non-border pixel in the image. For satellite images, κ is typically set to 2.

- Likewise, if the center pixel falls within region $R_{A'}$, that is $A' - \epsilon \leq x < \frac{A+A'}{2}$, then we select A'.

- If x is midway between A and A', we simply select the average of A and A'.

- Finally, if x is an outlier with respect to A and A' so that $x > A+\epsilon$ or $x < A'-\epsilon$, we leave x unchanged.

Thus, four values are computed from the four pairs of pixels surrounding the central pixel in the 3×3 window. In the following step, a mean of these four values is computed. Finally, the central pixel x is replaced by an average of the value computed in the previous step and the center pixel's original gray-level value. This latter average is similar to that of a damped gradient descent, which yields a faster convergence.

The SNF filter is applied three times on the input image with $\epsilon = 0$, $\epsilon = \kappa\sigma^*$, and $\epsilon = 0$. During the first run with $\epsilon = 0$, the input image is deblurred. When SNF is applied with $\epsilon = \kappa\sigma^*$, it essentially smoothens the pixels within a region and makes regions homogeneous. During the last run with $\epsilon = 0$, edges are sharpened. During each run several iterations are performed until, the pixel values remain unchanged between iterations. The resulting image has near-homogeneous regions with sharp transitions between bordering regions.

δ-Connected Components

A connected component in the image is a maximal collection of pixels with uniform reflectance such that a path exists between any pair of pixels in the component. Each pixel in the image will receive a label; pixels will have the same label if and only if they belong to the same connected component.

It is interesting to note that, in the previous paragraph, we defined connected components as a maximal collection of uniform color pixels such that a path existed between any pair of pixels. The conventional algorithm assumes that there is a connection between two adjacent pixels if and only if their gray-level values are identical. We relax this connectivity rule and present it as a more general algorithm called δ-Connected Components. In this approach we assume that two adjacent pixels with values x and y are connected if their absolute difference $|x - y|$ is no greater than the threshold δ. Note that setting the parameter δ to 0 reduces the algorithm to the classic connected components approach. Thus, a series of image segmentations can be performed by varying δ. The lowest level in the hierarchy computes the connected components with $\delta = 0$ for labeling the regions of the enhanced image. As δ increases, regions are merged together with respect to each region's decreasing similarity to its neighboring regions. Typical values of δ are set to $\kappa\sigma^*$, where κ and σ^* are the same as those input to enhancement filters.

To show the performance of our technique, we applied the image enhancement and segmentation algorithms to an image generated by principal component analysis of the six reflective bands of a LANDSAT TM image. Figure 4a shows the first principal component image, which explains 57% of the variability contained in the six reflective bands. Principal component images are commonly used to reduce the dimensionality of the input data (e.g. Singh and Harrison 1985). Image enhancement was performed (Figure 4b) by applying 4 iterations of SNF with $\epsilon = 0$ for de-blurring edges, 46 iterations with $\epsilon = 11$ used to flatten interior regions, and 68 iterations again with $\epsilon = 0$ used to sharpen the edges. Notice that the edges are enhanced, and different regions within the input image distinctly stand out. The enhanced image was then segmented using the connected component method with δ set to 11. Figure 4c shows the segmented image which contains 5,476 regions.

Thus, image segmentation is computationally intensive and requires both image enhancement and connected component labeling. Segmenting a single band of a large TM scene (with roughly 17 million pixels) would take roughly one hour and forty-five minutes on a single IBM RS6000 processor. Our research has produced image segmentation algorithms that scale well on a parallel computer. Using high performance computing techniques, the same segmentation of a remotely sensed image requires less than nine minutes on an IBM SP2 with 16 processors. (Bader et al. 1996, Bader and JaJa 1996b).

Our parallel implementation strategy can be described as follows. The input image, which is an $m \times n$ matrix of pixels, is divided in to a number of equal-sized tiles, which are assigned one per processor. A parallel algorithm consists of a sequence of local computations interleaved with communication steps, where computation and communications may overlap. Divide and conquer algorithms typically use a recursive strategy to split problems into smaller sub-problems and, given the solutions to these sub-problems, merge the results into the final solution. In our implementation, the computational tasks, especially the iterations during SNF enhancement phase are simplified by pre-fetching the neighborhood cells around the border of each tile in a coordinated fashion from neighboring processor's tile borders. Instead of communicating requests for individual pixels while computing at the borders of tiles, (where the needed pixels are owned by other processors) we created an augmented data structure called "ghost cells", which buffer the necessary pixels from adjacent tiles. Similarly, the communication between the processors is minimized by scheduling regular communication patterns and overlapping the transfer of border pixels with local computation. The code is written in C with the standard Message Passing Interface (MPI Forum 1995, 1997). MPI is both portable and efficient on most current high performance parallel machines, for example, the IBM SP2, Cray T3E, and SGI Origin 2000.

4 Retrieval of Bidirectional Reflectance Distribution Function (BRDF) From AVHRR Data at a Global Scale

Understanding land surface anisotropy is critical in remote sensing studies because measurements of surface reflectance are dependent upon the view and illumination geometry. The Bidirectional Reflectance Distribution Function describes the variations in reflectance with illumination and view geometry, and can be described as (Nicodemus et al. 1977):

$$f_r(\theta_s, \phi_s; \theta_v, \phi_v; \lambda) = \frac{dL(\theta_s, \phi_s; \theta_v, \phi_v; \lambda)}{dE(\theta_s, \phi_s; \lambda)} \tag{2}$$

Where f_r is the BRDF (sr^{-1}), dL is the reflected radiation for an incident beam of intensity dE at wavelength λ. θ and ϕ are the zenith and azimuth angles respectively. The subscripts s and v denote the angles in the sun and view directions respectively. BRDF is commonly expressed as the bidirectional reflectance factor $\rho = f_r \pi$.

Since most current remote sensing instruments such as AVHRR and TM record measurements at fixed illumination and view geometries at any given time, surface anisotropy could introduce errors in multitemporal analysis of these measurements unless they are corrected and normalized for consistent geometry (Holben 1986, Cihlar et al. 1994, Burgess and Pairman 1997). Researchers have shown that BRDF models can be used to infer surface properties such as the green leaf area index, and the amount of photosynthetically active radiation absorbed by plant canopies (Asrar et al. 1989, Myneni et al. 1995). THE BRDF information is also critical for deriving broad band albedo for climate and energy balance modeling (Pinker and Laszlo 1990). Therefore, understanding surface BRDF is important in studies of land cover dynamics.

Reflectance measurements from future Earth Observing System (EOS) sensors such as the Moderate Resolution Imaging Spectroradiometer (MODIS) and the Multi-angle Imaging Spectroradiometer (MISR) are expected to provide the capability to retrieve surface BRDF operationally through a combination of well tested algorithms (Strahler and Muller 1997, Diner et al. 1996). However, these algorithms have not been previously applied at a 'global scale', and there are several issues that need to be addressed:

- How do these algorithms perform at a global scale?
- What are the computational requirements? and how do we optimize the computational performance?

Our objective is to answer some of these questions by applying some of the BRDF algorithms chosen for MODIS and MISR to global AVHRR data.

Several studies aimed at deriving BRDF from AVHRR data have been reported in the literature (e.g. Cihlar et al. 1994, Braswell et al. 1996, Privette et al. 1996). However, unlike these studies which used samples of pixels from imagery at varying spatial and temporal resolution, we implemented two algorithms to retrieve BRDF from global AVHRR images which were generated by the NOAA/NASA Pathfinder program (James and Kalluri 1994).

From the suite of BRDF algorithms proposed to be implemented for MODIS and MISR instruments, we have chosen the modified Walthall model (Walthall et al. 1985, Nilson and Kuusk 1989) and the Coupled Surface-Atmosphere Reflectance Model (CSAR) (Rahman et al. 1993a) for deriving BRDF from AVHRR data. We believe that these two algorithms are good candidates for addressing the previously mentioned issues, since they have been shown to work well over different cover types (e.g. Rahman et al. 1993b, Lewis et al. 1995, Diner et al. 1996, Russell et al. 1995, O'Neill et al. 1997, Privette et al. 1997).

The modified Walthall model is an empirical model, which describes the surface BRDF as a quadratic function of view, solar and relative azimuth angles:

$$\rho(\theta_s, \theta_v, \phi, \lambda) = a_0(\theta_v^2 + \theta_s^2) + a_1\theta_v^2\theta_s^2 + a_2\theta_v\theta_s\cos\phi + a_3 \tag{3}$$

This model has 4 linear coefficients which are derived by a least square method using Gauss elimination technique (Stoer and Burlirsch 1993). ϕ is the relative azimuth angle ($\phi = \phi_v - \phi_s$). The only parameter in this model that has a physical meaning is a_3, and this parameter represents the nadir reflectances for an overhead sun.

A modified Minnaert function (Minnaert 1941), a one term Henyey and Greenstein function (Henyey and Greenstein 1941), and a hot spot function (Pinty et al. 1990) are used to describe the BRDF in the CSAR model with three unknown parameters ρ_0, k, and Θ:

$$\rho(\theta_s, \theta_v, \phi, \lambda) = \rho_0(\cos\theta_v \cos\theta_s(\cos\theta_v + \cos\theta_s))^{k-1} F(g)[1 + R(G)] \tag{4}$$

where

$$\begin{aligned} F(g) &= \frac{1 - \Theta^2}{[1 + \Theta^2 - 2\Theta\cos(\pi - g)]^{\frac{3}{2}}} \\ \cos g &= \cos\theta_s \cos\theta_v + \sin\theta_s \sin\theta_v \cos\phi \\ 1 + R(G) &= 1 + \frac{1 - \rho_0}{1 + G} \\ G &= [\tan^2\theta_v + \tan^2\theta_s - 2\tan\theta_v \tan\theta_s \cos\phi]^{\frac{1}{2}} \end{aligned}$$

ρ_0 represents nadir reflectances, and the parameter k indicates the level of surface anisotropy with a range of 0 to 1. A surface with lower values of k is more anisotropic than a surface with higher values of the same. Θ is a parameter that determines the relative amount of forward and backward scattering. The three unknown coefficients of the CSAR model (ρ_0, k, and Θ) are determined by model inversion and iteration.

The coefficients for both models are derived statistically for a set of observations measured at different view and illumination geometries. Since the AVHRR instrument measures reflectance over a given target only once a day, data from several days have to be used to get a good sampling of the BRDF at different view and solar angles. In our study, we used only the 10-day maximum value Normalized Difference Vegetation Index (NDVI) composite data acquired during the time period 1983 to 1986, since the maximum value compositing is shown to reduce the effects of clouds and atmosphere by choosing the clearest picture during the 10 day period (Holben 1986). Each 10 day composite image from the Pathfinder AVHRR Land (PAL) data set has calibrated reflectances and brightness temperatures from all the 5 bands of AVHRR, along with view and solar angles for each pixel at a spatial resolution of 8km. Cloud condition flags (CLAVR) are also present for each pixel, which were generated using a variety of tests (Stowe et al. 1991). The visible and near IR reflectances from AVHRR have been corrected for Rayleigh scattering and Ozone absorption. For a detailed description of the PAL data refer to (James and Kalluri 1994).

In order to isolate the influence of surface phenology in the BRDF signal, the input data was divided into four quarters: January-March, April-June, July-September, October-December. Our analysis indicate that increasing the temporal resolution by more than three months introduced phenological effects in the BRDF signal, while at the same time decreasing the time period by less than 3 months did not provide enough information to determine the BRDF accurately. Only clear pixels identified by the PAL cloud mask were used in the BRDF analysis, and the coefficients for both the modified Walthall model and the CSAR model were determined by inversion for the four quarters.

Each global composite image is an array of 5004 (2168 pixels. There are nine files for each composite, and we have processed data from 144 composite periods. Thus 1296 files were ingested, having a total volume of 27 Gbytes.

For the modified Walthall model, 3600 Floating Point Operations (FLOPs) are required per pixel to derive the coefficients. In comparison, the CSAR model is computationally more expensive because of its nonlinear nature, and requires 3.9 MFLOPs per pixel. Thus, for the 2.5 million land pixels in the PAL data set, 9 GFLOPs are required to solve the modified Walthall model, and 9750 GFLOPs are needed for the CSAR model. Given the peak performance of 266 MFLOPs per second of a single RS6000 processor, our estimates indicate that 3 hrs. of processing time would be required to determine the coefficients of the modified Walthall model using a single CPU. Using a single CPU requires 42 hrs. to solve the BRDF for the CSAR model.

To cut down the processing time, we implemented the two BRDF algorithms on the IBM SP2 machine previously described in Section 2. The input land data was evenly distributed among all the 16 nodes, and the communication between the processors was minimized. We achieved a performance rate of 0.9 GFLOPs/sec for the modified Walthall model, and 1.2 GFLOPs/sec for the CSAR model on the SP2, which significantly reduced the run time to 10 minutes for the modified Walthall model, and 2.5 hours to solve the CSAR It is clear from these results that our parallel implementation achieves an almost perfect linear speedup.

Although the CSAR model is more computationally intensive than the modified Walthall model, the results from both models are very similar for the data set we analyzed. Figure 5 shows the standard errors in channel 1 and 2 reflectances from the CSAR model and the modified Walthall model for the third quarter (July-September). The histograms of the standard errors show that both the models perform equally well at a global scale. However, since the model coefficients of the CSAR model are based on physical principles, these coefficients are closely related to the land cover type and provide more information about land cover dynamics compared to the model coefficients of the modified Walthall model (Zhang et al. 1998).

Figures 6a and 7a show the directional reflectances in channels 1 and 2 from the first 10 day composite in July 1983, and Figures 6b and 7b show the hemispherical albedo derived from the modified Walthall model for the same bands. The hemispherical albedo $[\rho(\theta_s, \lambda)]$ is derived by integrating the BRDF over the existence hemisphere for a single irradiance direction, and is a key parameter used in energy balance models:

$$\rho_h(\theta_s, \lambda) = \frac{1}{\pi} \int_0^{2\pi} \int_0^{\frac{\pi}{2}} \rho(\theta_s, \theta_v, \phi, \lambda) \cos\theta_v \sin\theta_v d\theta_v d\phi \tag{5}$$

The differences between directional reflectance and hemispherical albedo, expressed as a percentage of the hemispherical albedo are shown in Figures 6c and 7c for bands 1 and 2 respectively. It can be seen from figures 6c and 7c that the differences between directional reflectances and hemispherical albedo are large, especially in densely vegetated areas such as the tropical rain forests in South America and Central Africa, and in the temperate regions of Asia and Europe. Also, since visible reflectances are more anisotropic than NIR reflectances, these differences are larger in channel 1. Differences in channel 1 directional reflectance and hemispherical albedo are significant, having typical values of differences greater than 25% in vegetated areas indicating that the use of reflectances without BRDF correction could result in large errors in modeling land cover dynamics. Deserts on the other hand show smaller difference between directional reflectance and hemispherical albedo. Areas colored in red (Himalayas, Andes etc.) have null values since these areas were flagged as "cloudy" by CLAVR.

For the first time to our knowledge, we have demonstrated the feasibility of applying simple as well as complex BRDF algorithms at a global scale using high performance computing techniques. Results from this analysis are significant, since they not only provide us with valuable information about the performance of these algorithms chosen for MODIS and MISR at a global scale, but also help us in gauging the computational requirements to process large volumes of data operationally.

5 Designing a Database for Processing, Storing and Retrieving AVHRR Data

Several global data sets derived from the AVHRR instrument have been produced to study land cover dynamics since 1981. These include several versions of the Global Vegetation Index (GVI) products (Kidwell 1990, Goward et al. 1993, Goward et al. 1994, Gutman et al. 1994), the continental NDVI data set produced by the Global Inventory Monitoring and Modeling Studies (GIMMS) group at NASAs Goddard Space Flight Center (GSFC) (Holben 1986, Los et al. 1994), the Pathfinder AVHRR Land (PAL) data set (James and Kalluri 1994) and the 1 km. Global land data produced by the Earth Resources Observation Systems (EROS) Data Center (EDC) (Eidenshink and Faundeen 1994). A comprehensive review of these data is provided by Townshend (1994). Although these data sets have found widespread use in the earth system science community, they have several inherent limitations. Some of the limitations include availability of data in a fixed geographic projection, spatial and temporal resolution, with little or no capability for generating subsets based on user requirements. The compositing method and time interval are also static for all the previously mentioned AVHRR data sets. Some of these AVHRR data sets also have atmospheric correction applied to them. However, users who are interested in retrieving atmospheric properties from uncorrected satellite measurements and those users who want to experiment with new atmospheric correction algorithms may prefer to obtain uncorrected satellite data.

Because of the limitations of these data sets, the full potential capabilities of the AVHRR instrument cannot be exploited for special applications such as monitoring global Net Primary Production (NPP) (Prince and Goward 1995). Moreover, the requirements of users differ depending upon their specific application and usage of the data sets, and these requirements are expected to change as they gain experience in the use of these data sets and as their needs evolve (Townshend 1994). Thus, there is an important need to design a processing system that can generate AVHRR data sets following the specifications of individual users. Using the algorithms developed by the Pathfinder II group (El Saleous et al. 1998) we have designed an integrated processing system that can process, archive and distribute AVHRR data to the scientific community as per their individual data requirements.

An end to end design of a system to process AVHRR data tailored to different user requirements is a complex task, especially since the amount of the raw level 1B data is about 220 Gbytes per year. Moreover, to generate a data set suitable for studying land cover dynamics, several complex algorithms have to be applied to the raw data for navigation and geolocation of pixels, radiometric calibration, atmospheric correction, and compositing (Townshend et al. 1994). We have designed and built a comprehensive prototype system that allows the researchers to request and generate data according their needs by specifying:

- Region of interest
- Map projection
- Spatial resolution
- Temporal resolution
- Land/Ocean data
- Atmospheric correction
- Cloud screening
- Compositing function

Thus, the user would specify the spatial and temporal resolution, along with a compositing criterion (e.g. maximum NDVI) and the data would be generated in the geographic projection of his/her choice. Also, the user would have the option of either obtaining a data set corrected for atmospheric effects or just calibrated data. Either land or ocean data alone can be retrieved as well.

To achieve optimum performance, the system consists of two major components; the first involves processing modules that are common to all user queries, and the second involves general indexing, search and retrieval procedures in addition to a library of processing functions that will be unique to specific queries. The first stage can be considered as a preprocessing stage, and involves ingesting satellite orbits, precise navigation using satellite ephemeris, calibration of all the five AVHRR channels, determination of cloud condition information and data quality. Algorithms developed by El Saleous at al. (1998) have been used for pre processing level 1B data. Note that no gridding or resampling of the data is done during the preprocessing stage. Once the preprocessing is done, the data is indexed and placed on a disk array for fast retrieval and generation of user specified products. For each pixel the following parameters are stored: latitude and longitude, calibrated reflectances and brightness temperatures from the five bands of AVHRR, view and solar geometry, cloud and quality flags, and date and time of observation.

Our data indexing scheme is novel, and can be briefly as follows. We first create a two dimensional grid with a spatial resolution of $1^0 \times 1^0$. Each $1^0 \times 1^0$ cell can be considered as a "bucket" containing all the IFOVs that have been navigated into that region. Within each bucket all the pixels are indexed using an optimal *k-d* tree spatial data structure. The *k-d* tree data structure is a hierarchical spatial data structure in which the k dimensional space is recursively divided (Samet 1990). In our case, k represents a two dimensional space denoted by latitudes and longitudes. Thus, the $1^0 \times 1^0$ space is recursively divided in to finer regions hierarchically, based on latitudes and longitudes, and a binary search tree is constructed. Note that this indexing ensures that all the navigated IFOVs are preserved absolutely with no loss in information.

The *k-d* tree for our case can be described as follows. The first branch within the $1^0 \times 1^0$ tree represents the median latitude of all the pixels within the cell. All the pixels within the $1^0 \times 1^0$ cell are divided into two regions by the median latitude. Within each region further division is made by the median longitude of the pixels. Thus, the latitude and the longitude are used alternatively to decompose the entire space. Finally, a global index is created which can be used to retrieve the pixels for a given Cartesian coordinate. A detailed explanation of the *k-d* data structure can be found in (Bentley 1975). The *k-d* tree architecture is better for representing point data compared to other methods such as quadtrees (Samet 1989).

Once a user specifies a spatio-temporal query, the global index is searched and all the IFOV's that fall within the spatial bounding box specified by the user are retrieved. The next step is to do atmospheric correction and compositing based on user defined criterion. Our current version of implementation supports corrections for Rayleigh scattering, ozone and water vapor absorption, and stratospheric aerosols. After these corrections have been applied, then the data is binned in to one of the thirty one geographic projections supported by our processing system, using a nearest neighbor inverse binning algorithm (Emery et al. 1989, Cracknell 1997).

Once the data is ingested into the system, it takes 22 minutes on an IBM RS6000 to generate an AVHRR image with all the calibrated bands along with locational and geometry information for each pixel at a spatial resolution of 8 km for data from a single day. The image generated for our benchmark includes both land as well as ocean data. Although the current data base design is prototyped with AVHRR GAC data only, it can be further expanded to support geospatial raster data from other satellites as well. Storing the satellite data in a hierarchical data structure has significant advantages since it allows us to use the spatial and temporal metadata in a relational data base environment to perform Boolean searches and logical operations on multiple data sets using queries defined by the user.

6 Conclusions

In this paper we presented an overview of some of the high performance methodologies that we have implemented to study land cover dynamics. Algorithms we have developed are scalable and portable, and run on both serial as well as parallel architectures. Some of the applications are computationally intensive (e.g. atmospheric correction, image segmentation, and retrieval of BRDF), while others are more I/O bound (e.g. AVHRR data processing).

The high performance computing technology has matured to the point where most of the new high-end servers and workstations contain multiple processors that can be programmed using standard systems software. The technical challenge in handling our applications has been in improving the overall complexity and in mapping the computation into multiple processors in such a way as to ensure load balancing across the nodes and to minimize the overhead incurred by communication and synchronization. All of our computationally intensive algorithms achieve a linear speedup in terms of the number of processors available and, in addition, their sequential complexity is superior to any of the previously known implementations.

Our data-intensive applications, such as the on-demand generation of user-specified AVHRR data products, have required novel indexing schemes and particular data placement methods across the available disks so as to achieve the maximum possible parallel I/O throughput. These techniques are currently being generalized to handle a wide variety of spatial and temporal data sets, including the fusion of multiple data sets with different spatial and temporal resolutions. The current prototype system built especially for AVHRR GAAC Level 1B data provides an unprecedented flexibility in generating user-specified data products, which we hope to extend to handle data fusion and correlation for data sets from multiple sensors, especially data collected by future EOS satellites.

Although our examples show that significant improvements in processing speeds can be achieved by using high performance computing for processing satellite data, in practice, high performance computing comes at a certain cost. The learning curve for developing scalable parallel programs is steep, and a parallel computers runtime environment is more unpredictable compared to a single processor system (Pancake 1996). Due to these reasons, it is worthwhile to invest resources in developing parallel implementation of algorithms that are well understood and robust compared to those that are still in an experimental stages of development; otherwise the initial costly investment could be largely wasted.

Data sets from future EOS satellites are expected to have routine operational corrections for atmospheric effects and BRDF at a global scale. These corrections are crucial for studying land cover dynamics and are computationally intense. We have tried to address some of the issues at both the algorithm level as well as at the computational level. Our results show that unless innovative approaches are used, processing high resolution global data sets operationally is not practical. For the first time we are able to ingest and correct complete TM scenes within a few minutes for atmospheric effects. Classification of regions in remotely sensed imagery requires the computationally intensive tasks of image enhancement and segmentation. Our parallel version of the hierarchical connected component algorithm can segment a TM scene in minutes compared to a few hours on a high performance computer. The results from our BRDF study are unique since they provide us valuable information about the applicability, accuracy, and processing time of different algorithms at a global scale which was not previously available. Efficient access to massive spatial data bases such as global AVHRR data, and processing it in a real time mode requires engineering a processing system using a hierarchical data structure. The sequential hierarchical data structure that we used in designing the AVHRR database provides very efficient random search methods by capitalizing on the physical organization of the data. The results from our analysis are expected to provide new insights into the implementation of remote sensing algorithms at a global scale for studying land cover dynamics, and in the design of new processing methodologies using smart and innovative computational techniques.

7 Acknowledgements

This research has been made possible by a grant from the National Science Foundation (BIR9318183). David Bader was supported by the NSF CISE postdoctoral research associateship in experimental computer science (No. 96-25668). We wish to thank Jeff Masek for providing us with the Landsat computational requirements.

8 References

Acharya, A., Uysal, M., Bennett, R., Mendelson, A., Beynon, M., Hollingsworth, J., Saltz, J. and Sussman, A., 1996, Tuning the performance of I/O-intensive parallel applications. *Proceedings of the Fourth ACM Workshop on I/O in Parallel and Distributed Systems*, held in Philadelphia, on May 27 1996, 15-27.

Asrar, G., Myneni, R. B. and Kanemasu, E. T., 1989, Estimation of plant-canopy attributes from spectral reflectance measurements. In *Estimation of plant-canopy attributes from spectral reflectance measurements*, edited by G. Asrar, (New York:

John Wiley), 252-296.

Bader, D. A. and JaJa, J., 1996a, Parallel algorithms for image histogramming and connected components with an experimental study. *Journal of Parallel and Distributed Computing*, 35, 173-190.

Bader, D. A. and JaJa, J., 1996b, Practical parallel algorithms for dynamic data redistribution, median finding, and selection. *Proceedings of the 10th International Parallel Processing Symposium*, Honolulu, HI, 292-301.

Bader, D. A., JaJa, J., Harwood, D. and Davis, L. S., 1996, Parallel algorithms for image enhancement and segmentation by region growing with an experimental study. *The Journal of Supercomputing*, 10, 141-168.

Bentley, J. L., 1975, Multidimensional binary search trees for associative searching. *Communications of the ACM*, 18, 509-517.

Braswell, B. H., Schimel, D. S., Privette, J. L., Moore III, B., Emery, W. J., Sulzman, E. W. and Hudak, A. T., 1996, Extracting ecological and biophysical information from AVHRR optical data: An integrated algorithm based on inverse modeling. *Journal of Geophysical Research*, 101, 23335-233348.

Burgess, D. W. and Pairman, D., 1997, Bidirectional reflectance effects in NOAA AVHRR data. *International Journal of Remote Sensing*, 18, 2815-2825.

Castleman, K. R., 1996, *Digital Image Processing* (New Jersey: Prentice Hall).

Chandrasekhar, S., 1960. *Radiative Transfer* (New York: Dover).

Chang, Y. L. and Li, X., 1994, Adaptive image region-growing. *IEEE Transactions on Image Processing*, 3, 868-872.

Cihlar, J., Manak, D. and Voisin, N., 1994, AVHRR bidirectional reflectance effects and compositing. *Remote Sensing of Environment*, 48, 77-88.

Cracknell, A. P., 1997. *The advanced very high resolution radiometer (AVHRR)* (London: Taylor & Francis).

Diner, D. J., Davies, R., Varnai, T., Borel, C. and Gerstl, S. A. W., 1996, *MISR-Level 2 Top-of-Atmosphere albedo algorithm theoretical basis.* (JPL)
URL:http://eospso.gsfc.nasa.gov/atbd/misrtables.html..

Eidenshink, J. C. and Faundeen, J. L., 1994, The 1 km AVHRR global land data set: first stages in implementation. *International Journal of Remote Sensing*, 15, 3443-3462.

El Saleous, N. and Vermote, E., AVHRR Pathfinder II: improved algorithms to derive products for land investigations. *International Journal of Remote Sensing*(in press).

Emery, W. J., Brown, J. and Nowak, Z. P., 1989, AVHRR image navigation: Summary and review. *Photogrammetric Engineering and Remote Sensing*, 8, 1175-1183.

Fallah-Adl, H., JaJa, J., Liang, S., Townshend, J. R. G. and Kaufman, Y. J., 1996a, Fast algorithms for removing atmospheric effects from satellite images. *IEEE Computational Science and Engineering*, 3, 66-77.

Fallah-Adl, H., JaJa, J. and Liang, S., 1996b, Fast algorithms for estimating aerosol optical depth and correcting thematic mapper imagery. *The Journal of Supercomputing*, 10, 315-329.

Forster, B. C. and Best, P., 1994, Estimation of SPOT P-mode point spread function and derivation of a deconvolution filter. *ISPRS Journal of Photogrammetry and Remote Sensing*, 49, 32-42.

Fraser, R. S., Ferrare, R. A., Kaufman, Y. J., Markham, B. L. and Mattoo, S., 1992, Algorithm for atmospheric correction of aircraft and satellite imagery. *International Journal of Remote Sensing*, 13, 541-557.

Fraser, R. S. and Kaufman, Y. J., 1985, The relative importance of scattering and absorption in remote sensing. *IEEE Transactions on Geoscience and Remote Sensing*, 23, 625-633.

Goward, S. N., Dye, D. G., Turner, S. and Yang, J., 1993, Objective assessment of the NOAA Global Vegetation Index data product. *International Journal of Remote Sensing*, 14, 3365-3394.

Goward, S. N., Turner, S., Dye, D. G. and Liang, S., 1994, The University of Maryland improved Global Vegetation Index data set for terrestrial monitoring. *International Journal of Remote Sensing*, 15, 3365-3395.

Goward, S. N. and Williams, D. L., 1997, Monitoring the terrestrial biosphere: Landsat and Earth System Science. *Photogrammetric Engineering and Remote Sensing*, 63, 887-900.

Gutman, G. G., Ignatov, A. M. and Olson, S., 1994, Towards better quality of AVHRR composite images over land: reduction of cloud contamination. *Remote Sensing of Environment*, 50, 134-148.

Haralick, R. M. and Shapiro, L. G., 1985, Image segmentation techniques. *Computer Vision, Graphics, and Image Processing*, 29, 100-132.

Harwood, D., Subbarao, M., Hakalahti, H. and Davis, L. S., 1987, A new class of edge-preserving smoothing filters. *Pattern Recognition Letters*, 6, 155-162.

Henyey, L. G. and Greenstein, T. L., 1941, Diffuse radiation in the galaxy. *Astrophysical Journal*, 93, 70-83.

Holben, B., 1986, Characteristics of maximum-value composite images from temporal AVHRR data. *International Journal of Remote Sensing*, 7, 1417-1434.

James, M. E. and Kalluri, S. N. V., 1994, The Pathfinder AVHRR land data set: an improved coarse resolution data set for terrestrial monitoring. *International Journal of Remote Sensing*, 15, 3347-3364.

Kaufman, Y. J., 1984, The atmospheric effect on separatability of field classes measured from satellite. *Remote Sensing of Environment*, 18, 21-34.

Kaufman, Y. J. and Holben, B. N., 1996, Hemispherical backscattering by biomass burning and sulfate particles derived from sky measurements. *Journal of Geophysical Research*, 101, 19433-19445.

Kaufman, Y. J. and Sendra, C., 1988, Algorithm for automatic atmospheric corrections to visible and near-IR satellite data. *International Journal of Remote Sensing*, 9, 1357-1381.

Kaufman, Y. J. and Tanre, D., 1996, Strategy for direct and indirect methods for correcting the aerosol effect on remote sensing: from AVHRR to EOS-MODIS. *Remote Sensing of Environment*, 55, 65-79.

Kaufman, Y. J., Tanre, D., Remer, L. A., Vermote, E. F., Chu, A. and Holben, B. N., 1997, Operational remote sensing of tropospheric aerosols over land from EOS moderate resolution imaging spectroradiometer. *Journal of Geophysical Research*, 102, 17051-17067.

Kidwell, K. B., 1990, *Global Vegetation Index User's Guide* (Washington D.C.: NOAA/NESDIS, National Climatic Data Center).

Kneizys, F. X., Shettle, E. P., Abreau, L. W., Chetwynd, J. H., Anderson, G. P., Gallery, W. O., Selby, J. E. A. and Clough, S. A., 1988, *Users guide to LOWTRAN7* (Hanscom AFB, MA.: Airforce Geophysical Laboratory).

Lewis, P., Barnsley, M. J., Sutherland, M. and Muller, J.-P., 1995, Estimating land surface albedo in the HAPEX-Sahel Experiment: model-based inversion using ASAS. *International Geoscience and Remote Sensing Symposium*, Florence, Italy, July 10-14, pp. 2221-2223.

Liang, S., Fallah-Adl, H., Kalluri, S., Jaja, J., Kaufman, Y. J. and Townshend, J. R. G., 1997, An operational atmospheric correction algorithm for Landsat Thematic Mapper imagery over the land. *Journal of Geophysical Research*, 102, 17173-17186.

Los, S. O., Justice, C. O. and Tucker, C. J., 1994, A global $1^0 \times 1^0$ NDVI data set for climate studies derived from the GIMMS continental NDVI data. *International Journal of Remote Sensing*, 15, 3493-3518.

Message Passing Interface (MPI) Forum, 1995, *MPI: A Message-Passing Interface Standard* (Knoxville, TN: University of Tennessee).

Message Passing Interface (MPI) Forum, 1997, *MPI-2: Extensions to the Message-Passing Interface* (Knoxville, TN: University of Tennessee).

Minnaert, M., 1941, The reciprocity principle in lunar photometry. *Astrophysical Journal*, 93, 403-410.

Myneni, R. B., Maggion, S., Iaquinta, J., Privette, J. L., Gobron, N., Pinty, B., Kimes, D. S., Verstraete, M. M. and Williams, D. L., 1995, Optical remote sensing of Vegetation: modeling, caveats, and algorithms. *Remote Sensing of Environment*, 51, 169-188.

Nicodemus, F. E., Richmond, J. C., Hsia, J. J., Ginsberg, I. W. and Limperis, T., 1977, *Geometrical considerations and nomenclature for reflectance* (Washington D.C.:National Bureau of Standards).

Nilson, T. and Kuusk, A., 1989, A reflectance model for homogeneous plant canopies and its inversion. *Remote Sensing of Environment*, 27, 157-167.

O'Neill, N. T., Zagolski, F., Bergeron, M., Royer, A., Miller, J. R. and Freemantle, J., 1997, Atmospheric correction validation of casi images acquired over the Boreas southern study area. *Canadian Journal of Remote Sensing*, 23, 143-162.

Pancake, C. M. 1996, Is Parallelism for you? *IEEE Computational Science and Engineering*, 3, 18-36.

Pinker, R. T. and Laszlo, I., 1990, Improved prospects for estimating insolation for calculating regional evapotranspiration from remotely sensed data. *Agricultural and Forest Meteorology*, 52, 227-251.

Pinty, B., Verstraete, M. M. and Dickinson, R. E., 1990, A physical model of the bidirectional reflectance of vegetation canopies, 2. Inversion and validation. *Journal of Geophysical Research*, 95, 11767-11775.

Poropat, G. V., 1993, Effect of system point spread function, apparent size, and detector instantaneous field of view on the infrared image contrast of small objects. *Optical Engineering*, 32, 2598-2607.

Prince, S. D. and Goward, S. N., 1995, Evaluation of the NOAA/NASA Pathfinder AVHRR Land Data Set for global primary production. *International Journal of Remote Sensing*, 17, 217-221.

Privette, J. L., Emery, W. J. and Schimel, D. S., 1996, Inversion of a vegetation reflectance model with NOAA AVHRR data. *Remote Sensing of Environment*, 58, 187-200.

Rahman, H., Verstraete, M. M. and Pinty, B., 1993a, Coupled surface-atmosphere reflectance model (CSAR). 1. Model description and inversion against synthetic data. *Journal of Geophysical Research*, 98, 20791-20801.

Rahman, H., Pinty, B. and Verstraete, M. M., 1993b, Coupled surface-atmospheric reflectance (CSAR) model. 2. Semiempirical surface model usable with NOAA Advanced Very High Resolution Radiometer. *Journal of Geophysical Research*, 98, 20791-20801.

Russell, C. A., Walthall, C. L., Irons, J. R. and Brown de Colstoun, E. C., 1995, Comparison of airborne and surface spectral bidirectional reflectance factors, spectral hemispherical reflectance and spectral vegetation indices. *Journal of Geophysical Research*, 100, 25509-25522.

Samet, H., 1989. *The Design and Analysis of Spatial Data Structure* (Reading: Addison Wesley).

Samet, H., 1990. *Applications of Spatial Data Structures Structure* (Reading: Addison Wesley).

Sellers, P. J., Hall, F. G., Asrar, G., Strebel, D. E. and Murphy, R. E., 1992, An overview of the First international land surface climatology project (ISLSCP) field experiment (FIFE). *Journal of Geophysical Research*, 97, 18345-18371.

Singh, A. and Harrison, A., 1985, Standardized principal components. *International Journal of Remote Sensing*, 6, 883-896.

Singh, S. M. and Saull, R. L., 1988, The effect of atmospheric correction on the interpretation of multitemporal AVHRR-derived vegetation index dynamics. *Remote Sensing of Environment*, 25, 37-51.

Stoer, J. and Burlirsch, R., 1993. *Introduction to Numerical Analysis* (New York, Springer-Verlag).

Stowe, L. L., McClain. E. P., Carey, R., Pellegrino, P., Gutman, G. G., Davis, P., Long, C. and Hart, S., 1991, Global distribution of cloud cover derived from

NOAA/AVHRR operational satellite data. *Advances in Space Research*, 3, 51-54.

Strahler, A. H. and Muller, J., 1997, *MODIS BRDF/Albedo Product: Algorithm Theoretical Basis Document* (Version 3.2). URL: http://eospso.gsfc.nasa.gov/atbd/modistables.html

Tanre, D., Holben, B. N. and Kaufman, Y. J., 1992, Atmospheric correction algorithm for NOAA-AVHRR products: Theory and applications. *IEEE Transactions on Geoscience and Remote Sensing*, 30, 231-248.

Townshend, J. R. G., Cushine, J., Hardy, J. R., and Wilson, A., 1988, *Thematic Mapper Data* (Swindon: National Environment Research Council)

Townshend, J. R. G., 1994, Global data sets for land applications from the Advanced Very High Resolution Radiometer: An introduction. *International Journal of Remote Sensing*, 15, 3319-3332.

Townshend, J. R. G., Justice, C. O., Skole, D., Malingreau, J. P., Cihlar, J., Teillet, P., Sadowski, F. and Ruttenburg, S., 1994, The 1 km resolution global data set: needs of the International Geosphere Biosphere Programme. *International Journal of Remote Sensing*, 15, 3417-3441.

Vermote, E. F., Tanre, D., Deuze, J. L., Herman, M. and Morcrette, J., 1997, Second simulation of the satellite signal in the solar spectrum, 6S: An overview. *IEEE Transactions on Geoscience and Remote Sensing*, 35, 675-686.

Walthall, C. L., Norman, J. M., Welles, J. W., Campbell, G. and Blad, B. L., 1985, Simple equation to approximate the bidirectional reflectance from vegetated canopies and bare soil surfaces. *Applied Optics*, 24, 383-387.

Westman, T., Harwood, D., Laitinen, T. and Pietikaeinen, M., 1990, Color segmentation by hierarchical connected components analysis with image enhancement by symmetric neighborhood filters. *Proceedings of the 10th International Conference on Pattern Recognition*, Atlantic City, NJ, 796-802.

Zhang, Z., Kalluri, S., JaJa, J., Liang, S. and Townshend, J. R. G., 1998, High performance algorithms for global BRDF retrieval. IEEE Computational Science and Engineering (in press).

Figure Captions

Figure 1. (a) A Red Green Blue (RGB) color composite of the visible bands (3, 2 and 1) of a TM scene over Maryland, USA, before atmospheric correction. The acquisition date of this scene is 29 August 1993 and the size of the image shown here is 512 pixels by 512 lines (b) A composite of the visible bands after atmospheric correction. (c) Band 1 (Blue) optical thickness image derived from the atmospheric correction algorithm

Figure 2. A 3×3 neighborhood of pixels. The symmetric pairs around the central pixel x, have the same letter.

Figure 3. Selection criteria for the SNF filter.

Figure 4. (a) First principal component image derived from the six reflective bands of TM. (b) Output image after SNF filtering. (c) Segmentation results

Figure 5. Histograms of standard errors in channel 1 and 2 reflectances derived from the Modified Walthall model and the CSAR model for the third quarter (July-September).

Figure 6 (a) Channel 1 (visible) reflectances from the 10 day Pathfinder AVHRR Land data set (July 1-10, 1983). (b) Hemispherical albedo for the same time period derived by integrating the modified Walthall model (equation 5). (c) The differences between directional reflectances (fig. 6a) and hemispherical albedo (6b) expressed as a percentage of the hemispherical albedo.

Figure 7 (a) Channel 2 (NIR) reflectances from the 10 day Pathfinder AVHRR Land data set (July 1-10, 1983). (b) Hemispherical albedo for the same time period derived by integrating the modified Walthall model (equation 5). (c) The differences between directional reflectances (fig. 7a) and hemispherical albedo (7b) expressed as a percentage of the hemispherical albedo.

Table 1. Landsat Thematic Mapper (TM) bands and their spectral wavelength intervals (Townshend et al. 1988)

TM Band No.	Wavelength interval (μm)
1	0.45-0.52
2	0.52-0.60
3	0.63-0.69
4	0.76-0.90
5	1.55-1.75
7	2.08-2.35
6	10.4-12.5

Figure 1a

Figure 1b

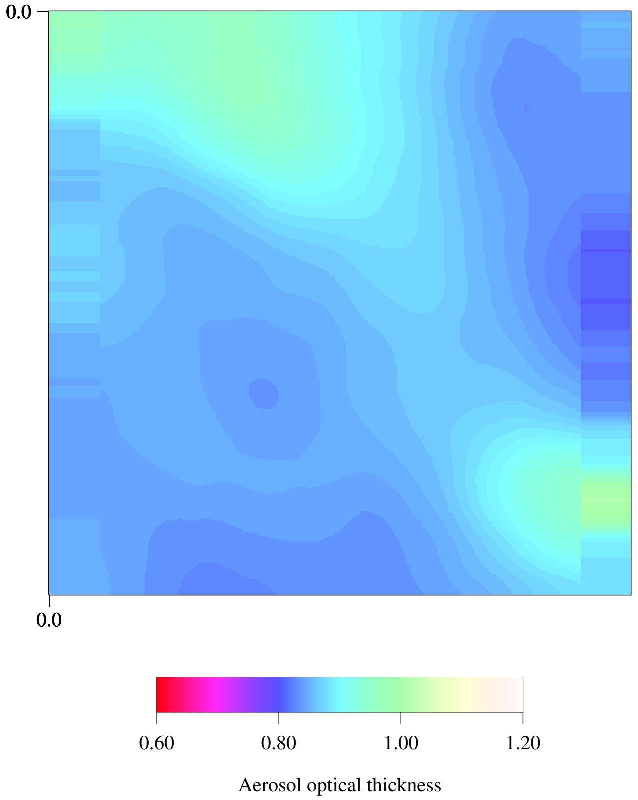

Figure 1c

Figure 2

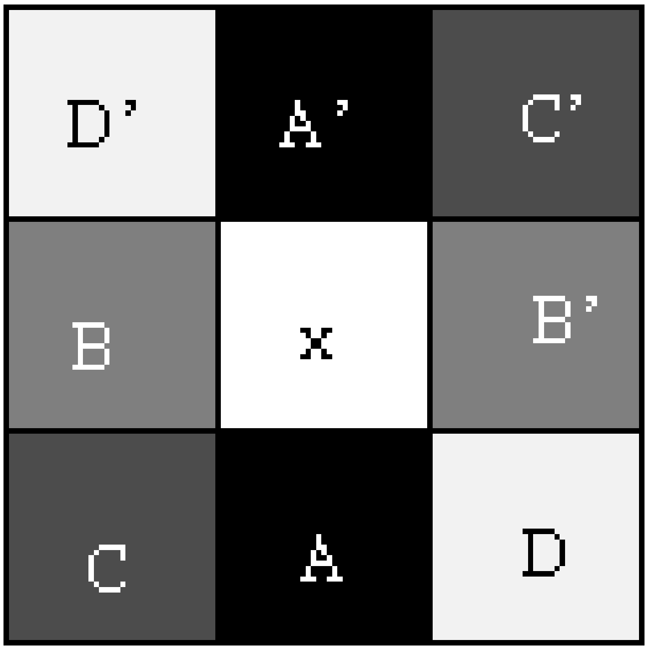

Figure 3

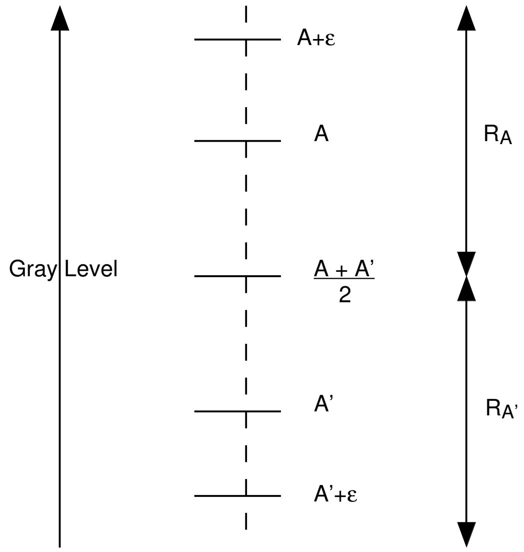

Figure 4a

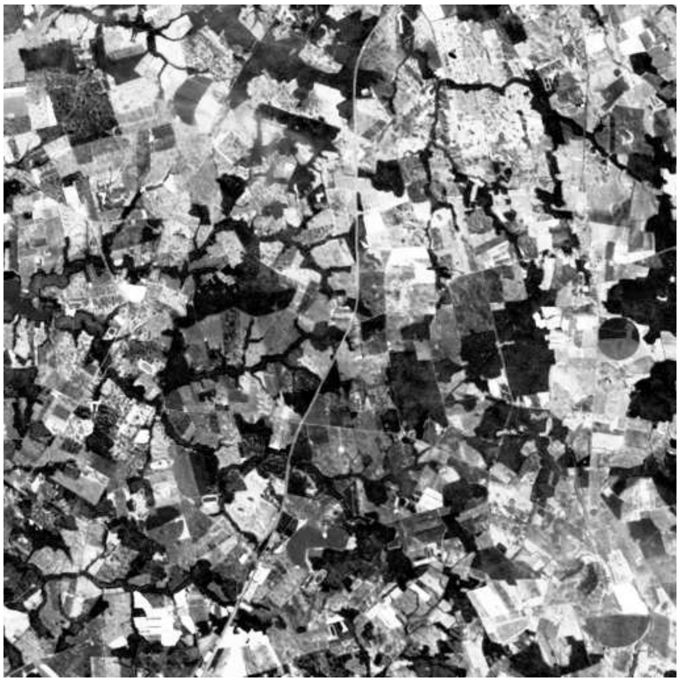

Figure 4b

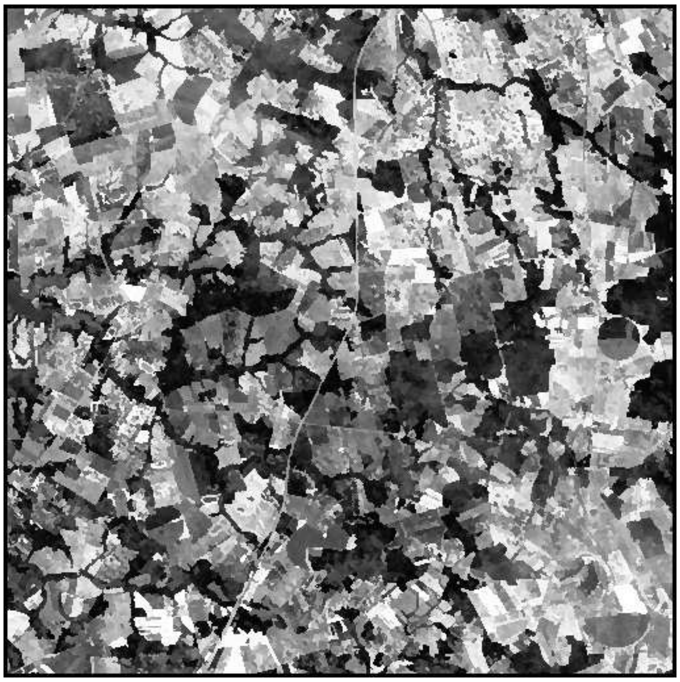

Figure 4c

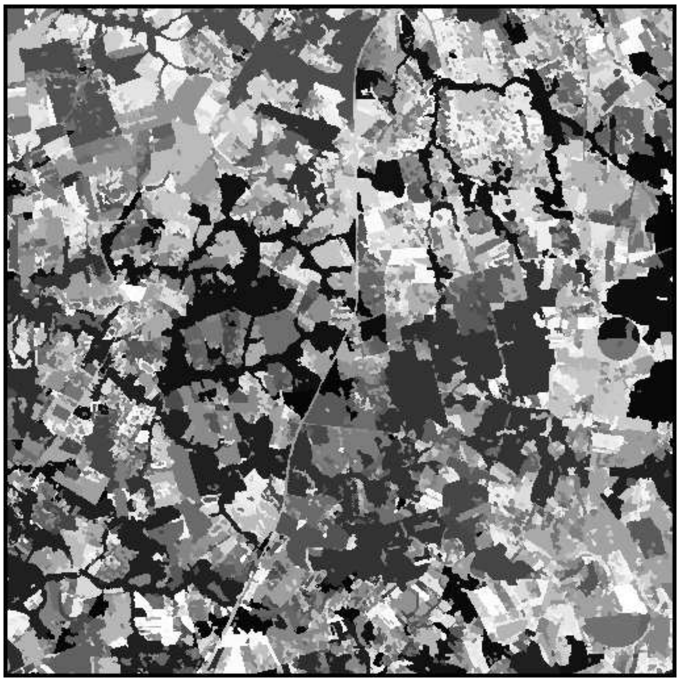

Figure 5

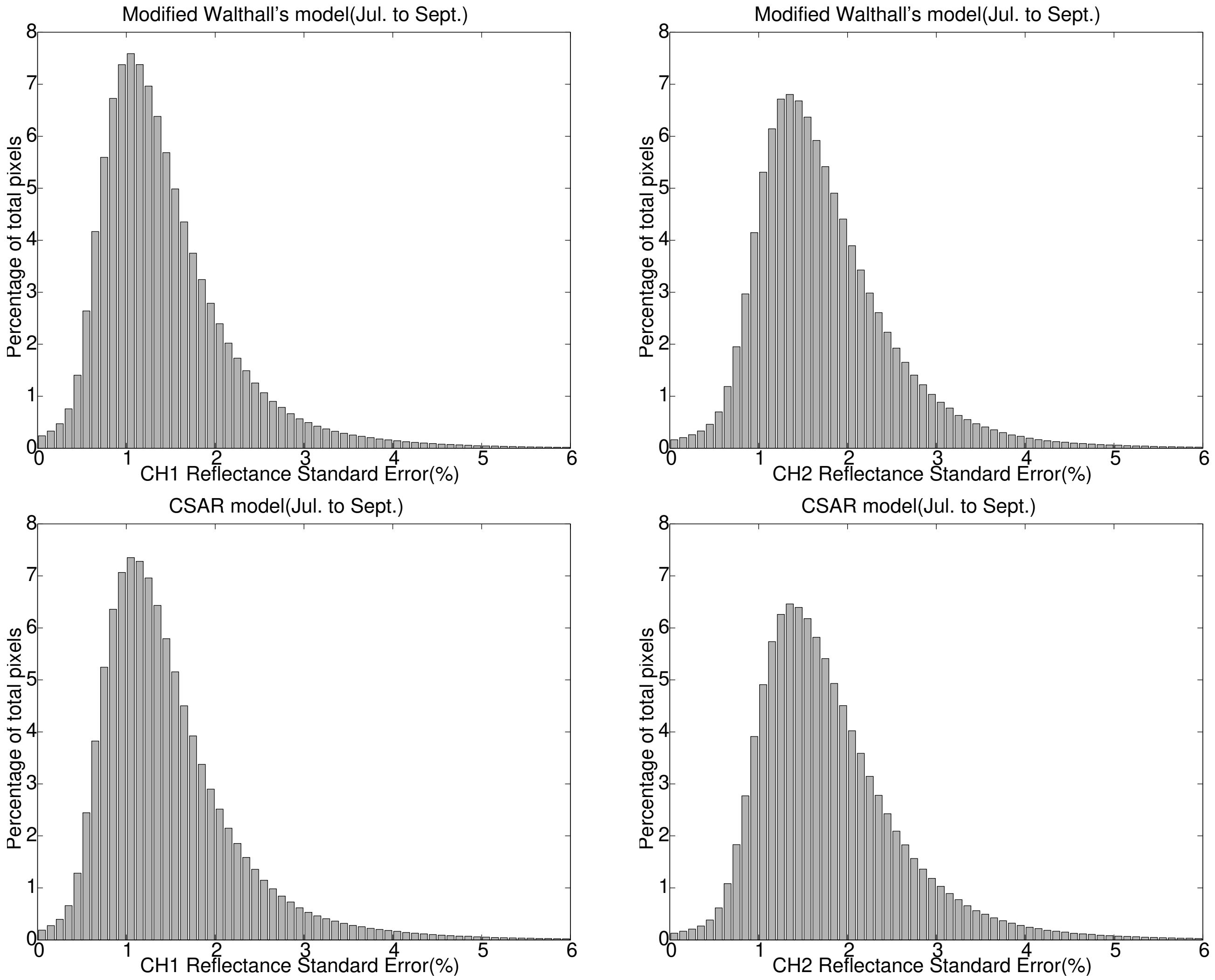
Modified Walthall's model(Jul. to Sept.)
Percentage of total pixels
CH1 Reflectance Standard Error(%)
Modified Walthall's model(Jul. to Sept.)
Percentage of total pixels
CH2 Reflectance Standard Error(%)
CSAR model(Jul. to Sept.)
Percentage of total pixels
CH1 Reflectance Standard Error(%)
CSAR model(Jul. to Sept.)
Percentage of total pixels
CH2 Reflectance Standard Error(%)

Figure 6a

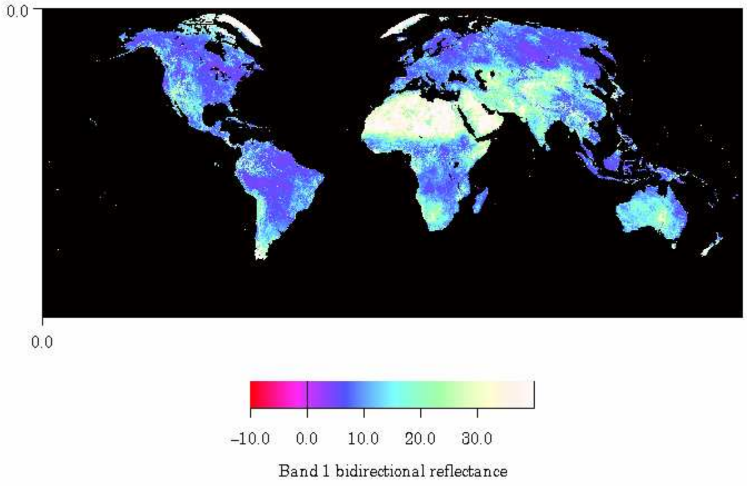

Figure 6b

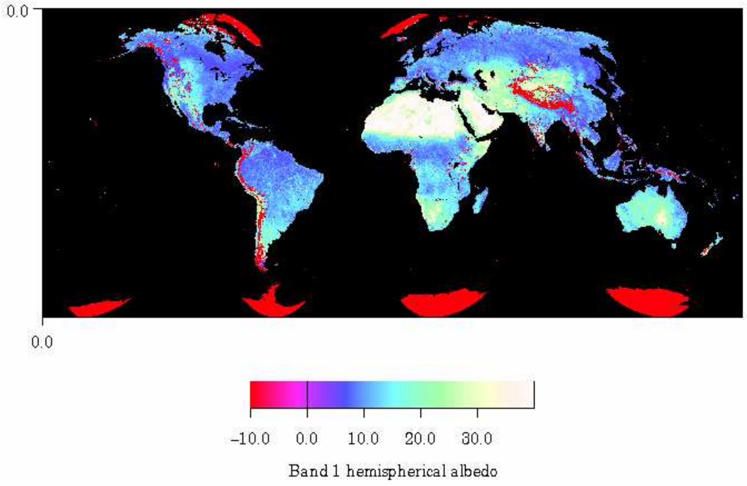

Figure 6c

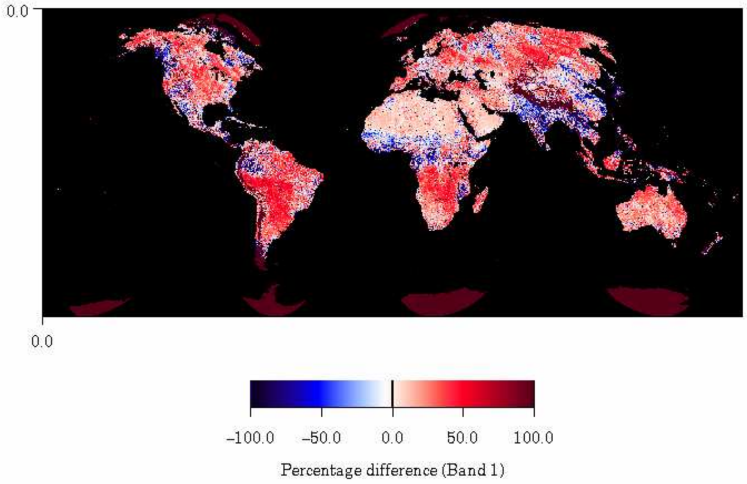

Figure 7a

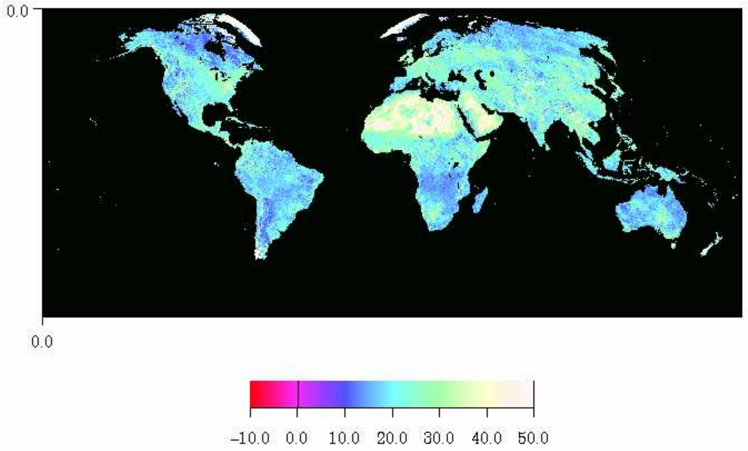

Band 2 bidirectional reflectance

Figure 7b

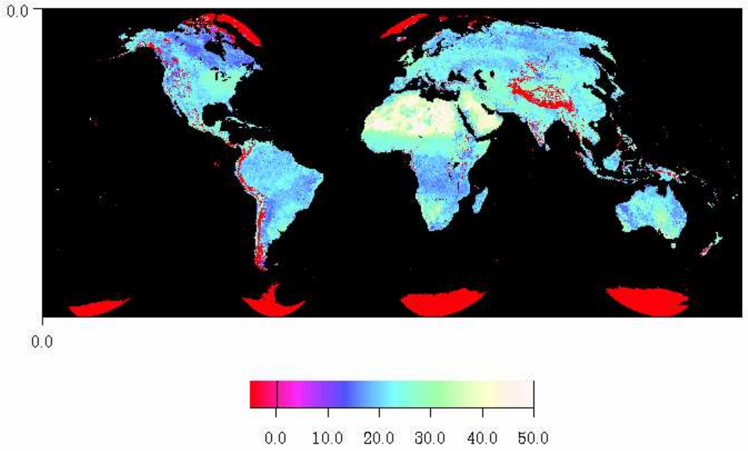

Band 2 hemispherical albedo

Figure 7c

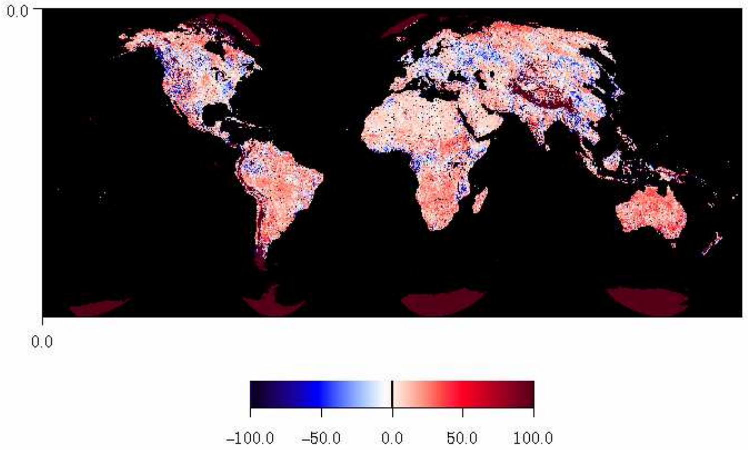

Percentage difference (Band 2)